UNIVERSITY OF BIRMINGHAM

Electrochemically decorated iridium electrodes with WS$_{3-x}$ toward improved oxygen evolution electrocatalyst stability in acidic electrolytes

Escalera-López, Daniel; Jensen, Kim D.; Rees, Neil V.; Escudero-Escribano, María

[Link to publication on Research at Birmingham portal](#)

Electrochemically-decorated iridium electrodes with WS$_{3-x}$ towards improved oxygen evolution electrocatalyst stability in acidic electrolytes

*Daniel Escalera-López[a,b], Kim Degn Jensen[c], Neil V. Rees[*a], and María Escudero-Escribano[*c]*

E-mail (N.V.R, M. E.-E.): n.rees@bham.ac.uk, m.escudero@chem.ku.dk

Dr. Daniel Escalera-López, Dr. Neil V. Rees
[a]Centre for Hydrogen and Fuel Cell Research, School of Chemical Engineering, University of Birmingham, Birmingham, B15 2TT, United Kingdom

Current address for D.E-L:
[b]Helmholtz-Institute Erlangen-Nürnberg for Renewable Energy (IEK-11), Forschungszentrum Jülich GmbH, Egerlandstraße 3, 91058, Erlangen, Germany

Dr. Kim Degn Jensen, Prof. Dr. María Escudero-Escribano
[c]Department of Chemistry, Nano-Science Center, University of Copenhagen, Universitetsparken 5, DK-2100, Copenhagen Ø, Denmark

[a]   Dr. D. Escalera-López, Dr. N. V. Rees
        Centre for Hydrogen and Fuel Cell Research
        School of Chemical Engineering, University of Birmingham,
        Birmingham, B15 2TT, United Kingdom
        E-mail: n.rees@bham.ac.uk
[b]   Helmholtz-Institute Erlangen-Nürnberg for Renewable Energy (IEK-11)
        Forschungszentrum Jülich GmbH, Egerlandstraße 3
        91058, Erlangen, Germany
[c]   Dr. K. D. Jensen, Prof. M. Escudero-Escribano
        Department of Chemistry
        Nano-Science Center
        University of Copenhagen, Universitetsparken 5,
        DK-2100, Copenhagen Ø, Denmark
        E-mail: m.escudero@chem.ku.dk

        Supporting information for this article is given via a link at the end of the document.

Iridium and its oxide, currently the state-of-the-art oxygen evolution reaction (OER) electrocatalyst in acidic electrolytes, is a cost-intensive material which undergoes significant corrosion under long-term OER operation. Thus, numerous researchers have devoted their efforts to mitigate iridium corrosion by decoration with corrosion-resistant metal oxides and/or supports to maximize OER catalysts durability whilst retaining its high activity.

Herein we propose a one-step, facile electrochemical route to obtain improved IrO_x thin film OER stabilities in acidic environments by decorating with amorphous tungsten sulphide (WS_{3-x}) upon electrochemical decomposition of a $[WS_4]^{2-}$ aqueous precursor. The rationale behind applying such WS_{3-x} decoration stems from the generation of a tungsten oxide phase at electro-oxidative potentials, a well-known corrosion-resistant photoactive OER catalyst.

This thorough study of the $[WS_4]^{2-}$ electrochemical decomposition on Ir electrodes demonstrates the viability of the proposed WS_{3-x} decoration, allowing the tailoring of experimental parameters responsible for WS_{3-x} nanoparticle size and surface coverage. OER stability tests coupled by ex-situ SEM and XPS corroborate the beneficial effect of WS_{3-x} decoration, yielding improved OER specific activity metrics along with minimized Ir surface roughening; a characteristic of electrodissolution. Iridium decoration with electrodeposited, corrosion-resistant oxides is consequently shown to be a promising route to maximize OER stabilities.

1. Introduction

The ongoing trend towards decarbonising of the energy sector has propelled the efforts to sustainably produce carbon-free energy vectors such as hydrogen.[1]–[5] A simple method to do so is via water splitting, which can be driven by renewable energy sources (e.g. solar photovoltaics, wind, hydroelectric) coupled to an electrochemical device such as a water electrolyser.[6] Electrolysers are a well-established technology proven to be extremely robust in alkaline media, with reported lifetimes over 15 years and reasonable conversion efficiencies of >50%.[7][8] Proton exchange membrane electrolysers, which operate in acidic media, on the other hand, have the potential of producing higher purity pressurised hydrogen at increased power densities than in alkaline conditions.[6][9][10] However, its commercial viability is hampered by the catalyst materials employed for the kinetically-hindered 4-electron oxygen evolution reaction (OER) taking place at the electrolyser anode.[11]–[13] In particular, the harsh electrochemical environments under which OER electrocatalysts operates severely narrows down the potential candidates to scarce Ir-based electrocatalysts.[14][15] These metals, and to a lesser extent their rutile-type oxide analogues, still undergo electrochemical dissolution during OER operation.[16]–[18] This dissolution is crucial for describing performance losses in PEM water electrolysers.[19][20] It has recently been shown that OER stability is not only highly dependent on their native structure and chemical environment,[21][22] but also on the degree of nanostructuring and surface defects.[23]–[25] Consequently, research into improving Ir catalyst utilization is extensive. Such improvement can be attempted through many different approaches; either by surface area maximization (e.g. nanoframes,[26][27] nanowires,[28] nanodendrites[29] and self-supported nanostructured networks[30]), by reducing loadings by use of mixed metal oxides,[31]–[34] or by anchoring to corrosion-resistant supports such as ATO[35]–[38] or TiO2[39][40] to yield stabilizing support interactions. Iridium anchoring to tin-based

electrocatalyst supports such as ATO or ITO, however, has been shown to be somewhat compromised by the inherent tin instability within the supports.[41] Simultaneously, the quest of finding alternative acid-stable OER electrocatalyst is ongoing and has recently been assessed by both high-throughput computational methods[42][43] or using various transition metal or complex non-noble metal compounds such as pyrochlores[44] or polyoxometalates.[45].

An elegant alternative to the investigation of such complex systems for improved OER concerns the fabrication of metal oxide-passivated IrO_x surfaces. Techniques such as magnetron sputtering, calcination or plasma jet oxidation[46]–[48] have been used for such investigations, but are generally very cost-intensive in terms of equipment which may ultimately limit their real world applicability. Electrochemical deposition is, conversely, an inexpensive and facile approach to decorate conductive surfaces up to the atomic nanocluster domain.[49]–[52] Besides the well-known conventional electrodeposition methods (such as cyclic voltammetry (CV), chronoamperometry or chronopotentiometry), pulsed electrodeposition (PE) allows nuclei formation with higher degree of monodispersion (i.e. narrower size distribution), with sizes and coverages modulated by the magnitude and duration of the pulses.[53]

We herein report a pulsed electrodeposition-based approach to decorate iridium thin film surfaces with transition metal oxides. A particular mode of PE, known as *pulse reverse potential/current* (i.e. double anodic-cathodic potential/current pulses) is selected, consisting on alternating anodic and cathodic pulses of equivalent magnitude and duration. To validate our approach, an electrodeposition bath containing a tungsten-based precursor, namely $[WS_4]^{2-}$, was utilized.[54]–[56] The successful decoration of WS_{3-x} onto the Ir thin film electrodes is evaluated by joint ex-situ scanning electrode microscopy (SEM) and X-ray photoelectron spectroscopy (XPS) studies, followed by short and long-term OER tests in acidic electrolyte to monitor activity and stability metrics after surface decoration. The foreseen conversion of WS$_{3-}$

$_x$ to the acid-resistant WO_3 at anodic potentials exerted during OER measurements,[57]–[59] following thermodynamic predictions based on the Pourbaix diagrams,[60] aims here to alleviate Ir electrodissolution at OER potentials by selectively protecting the thin film surface defects.[61] Ir-W mixed alloy systems, both in nanoparticulate[29] and nanocomposite configurations,[62] have indeed been recently explored as oxygen evolution electrocatalysts with improved activities ascribed to a wkening of the oxygen adsorbate intermediates, but also to significantly improved Ir stabilities under single-membrane electrode assembly configurations. The electrochemical decoration strategy employed here, thus, aims to stabilize a pure Ir phase with an acid-stable WO_3 nanoparticulate overlayer without the need to achieve metal phase intermixing, and consequently could be implemented to any Ir-based electrocatalyst.

2. Results and Discussion

2.1 Electrochemical deposition of amorphous tungsten sulphide on iridium

2.1.1 Electrochemistry of Ir substrate and $[WS_4]^{2-}$ precursor

The viability of the electrochemical synthesis of WS_{3-x} by decomposition of an aqueous $[WS_4]^{2-}$ precursor was investigated for Si/Cr/Ir electrodes (see Experimental for further details about electrode fabrication). Figure 1 shows a set of representative CVs obtained after continuous cycling from 0 V to 2.5 V vs. RHE in aqueous electrolytes in the absence (0.1 M $NaClO_4$, Figure 1a) and in presence (10mM $(NH_4)_2[WS_4]$ in 0.1 M $NaClO_4$, Figure 1b) of the aqueous $[WS_4]^{2-}$ precursor.

In 0.1 M $NaClO_4$, continuous cycling of the Si/Cr/Ir electrode gradually shows the irreversible conversion of polycrystalline metallic iridium to IrO_x (further information on the voltammetric regions I-IV labelled in Figure 1b can be found Section 1.1 ESI). Briefly, the characteristic monoatomic hydrogen underpotential deposition (H_{upd}) of metallic Ir (I) fades upon continuous

cycling to reveal both Ir^{3+} hydroxide $\rightleftharpoons$ Ir^{4+} (III) and Ir^{4+} hydrous oxide $\rightleftharpoons$ Ir^{5+} complex (IV)redox transitions.[63]–[66]

For the $[WS_4]^{2-}$-containing electrochemical bath, a broad electro-oxidative peak centred at ca. 2 V vs. RHE is observed, followed by a cathodic feature with an onset at ca. 0.4 V vs. RHE and peak at ca. -0.25 V, as shown in Figure 1c. Interestingly, both redox features present pseudo-stationary peak currents after the initial cycle, irrespective of the number of cycles. These electrochemical features are analogous to those obtained upon WS_{3-x} thin film electrodeposition by continuous oxidative-reductive cycling in glassy carbon electrodes.[55] XPS spectra obtained for Ir samples after undergoing 25 cycles within the -0.4 to 2.3 V vs. RHE voltage range (Figure 2a-c) provide insight on the electrochemically-driven oxidative-reductive $[WS_4]^{2-}$ decomposition. A W $4f_{7/2}$:$4f_{5/2}$ spin-orbit doublet with binding energies of ca. 32.3 and 34.5 eV is identified in the W $4f$ spectrum (Figure 2a), characteristic of W^{4+} species as expected for WS_{3-x}.[55] The prominent band centred at ca. 166 eV in the S $2p$ spectrum (Figure 2b) denotes the presence of oxidized sulfur moieties (SO_x^{y-}), most likely arising from the low stability towards environment exposure of the S^{2-}/S_2^{2-} moieties during sample transportation and storage. This have been observed to a lesser extent for MoS_x thin films.[67] The sole presence of one Ir $4f_{7/2}$:$4f_{5/2}$ spin-orbit doublet in the Ir $4f$ spectrum, at binding energies of ca. 60.2 and 63.3 eV (Figure 2c), indicates that the outermost Ir surface is predominantly found in its metallic state. These results lead us to believe that a WS_{3-x} film is successfully obtained after oxidative-reductive cycling, but ultimately converts to WO_2 after long-term atmosphere exposure.
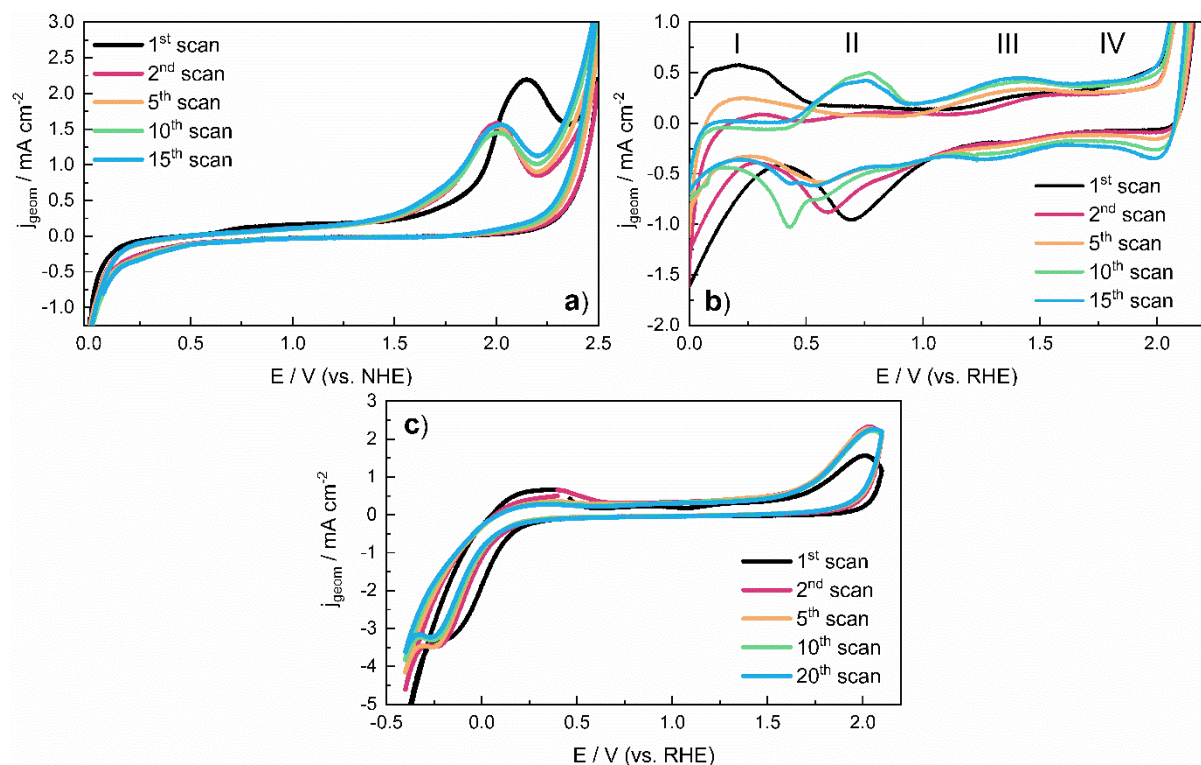
Figure 1. Representative voltammograms obtained on 0.25 cm^2 Si/Cr/Ir electrodes by continuous voltage cycling from 0 V to 2.5 V vs. RHE in a) 10 mM $(NH_4)_2[WS_4]$, 0.1 M $NaClO_4$ and b) 0.1 M $NaClO_4$ electrolytes; c) is analogous to a) using a voltage cycling window from -0.4 to 2.1 V vs. RHE (starting potential: 0.4 V). Scan rate: 50 mV s^{-1}.
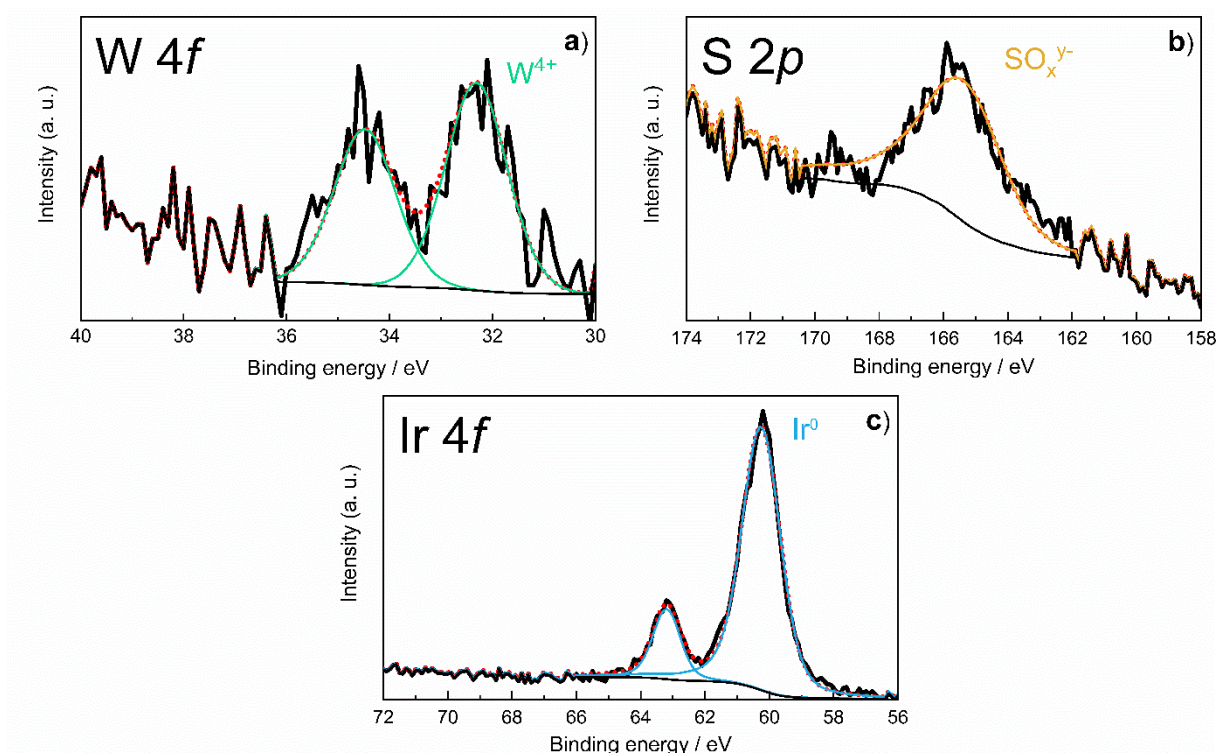
Figure 2. XPS spectra of a) W *4f*, b) S *2p* and c) Ir *4f*. Labels: W^{4+} *$4f_{7/2:5/2}$* (green), S *$2p_{3/2:1/2}$* (SO_x^{y-}, yellow), Ir^0 *$4f_{7/2:5/2}$* (blue), cumulative spectra (red).

Further voltammetric analysis indicates an evident suppression of the inherent electrochemical features of Ir, corroborated when overlapping the first (Figure 3a) and 15th (Figure 3b) voltammetric cycles obtained in the aforementioned electrolytes. The sharp and high-current OER electrocatalytic feature with onset at ca. 2.0 V vs. RHE and the H_{upd} desorption feature in the 0.0-0.5 V vs. RHE region, the most characteristic features for metallic Ir, are no longer present when cycling in presence of the $[WS_4]^{2-}$ precursor, similarly to features related to IrO_x formation (see insets Figure 3). We thus conclude, supported by the XPS results outlined earlier, that WS_{3-x} electrodeposition is also feasible on Ir surfaces, which we presume is substrate-independent, in consonance to previous electrode-dependent investigations of MoS_3 electrodeposition.[68]–[70] In addition, inherent Ir electroactivity suppression suggests that the

8

oxidative-reductive cycling deposition mechanism proceeds through a surface-bound pathway which somehow prevents electroadsorption of other aqueous species (namely H^+ and OH^-).
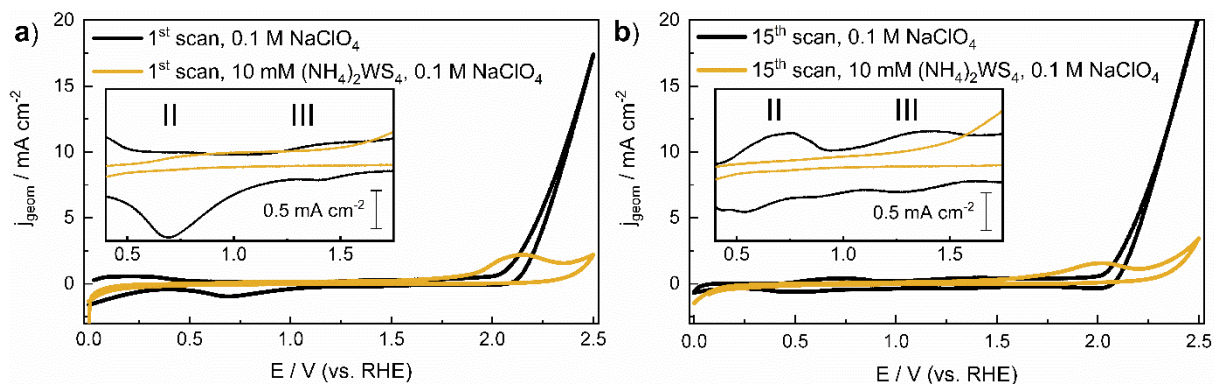
Figure 3. Representative a) first and b) 15th (dark yellow) voltammograms obtained by continuous cycling within the 0 V to 2.5 V vs. RHE electrochemical window for 0.25 cm^2 Si/Cr/Ir electrodes in 0.1 M NaClO$_4$ (black) and 10 mM (NH$_4$)$_2$[WS$_4$], 0.1 M NaClO$_4$ (dark yellow) electrolytes. Insets: zoom-in of the first and 15th voltammograms in the 0.4 to 1.80 V vs. RHE window. Scan rate: 50 mV s^{-1}.

To further corroborate this observation, we evaluated the influence of the voltage cycling window in the [WS$_4$]$^{2-}$-related electrochemical features. CVs recorded from 0 to 1.6 V vs. RHE (Figure 4a), where the upper vertex potential precedes the onset of the [WS$_4$]$^{2-}$ electro-oxidative event, present two cathodic pre-catalytic peaks (at ca. 0.13 and 0.33 V vs. RHE, respectively) equivalent to those found for H$_{upd}$ on pristine Ir electrodes.[71] This, in conjunction with the absence of the cathodic feature previously found for the oxidative-reductive cycling treatment, indicates that [WS$_4$]$^{2-}$ does not undergo any electrochemical reduction unless it is preceded by an electro-oxidative step. Alternatively, if CVs are recorded from 0.4 to 2.2 V vs. RHE (Figure 4b), where the lower vertex potential is higher than the onset of the [WS$_4$]$^{2-}$ reduction step, the broad [WS$_4$]$^{2-}$ electro-oxidative peak disappears. Such feature is gradually replaced by the

anodic current profile characteristic of OER, which would suggest a suppression of the $[WS_4]^{2-}$ electro-oxidation on Ir. Consequently, selective cycling in the oxidative range leads to de-activation of the $[WS_4]^{2-}$ anodic deposition pathway, which can be reinstated when cycling towards cathodic currents. This behaviour mirrors that found by Tan et al. for $[WS_4]^{2-}$ electrodeposition on glassy carbon substrates,[55] proposing a plausible electrodeposition mechanism, outlined below:

Oxidative adsorption:
$$[WS_4]^{2-} \rightarrow WS_3 + 1/8\, S_8 + 2e^- \quad (1)$$

WS$_3$ to WS$_2$ reductive conversion: $WS_3 + 2\,H^+ + 2e^- \rightarrow WS_2 + H_2S \qquad (2)$

Reductive desorption:
$$WS_3 + 1/8\, S_8 + 2e^- \rightarrow [WS_4]^{2-} \qquad (3)$$
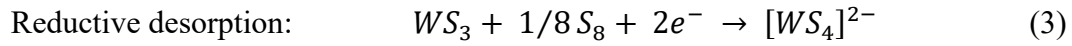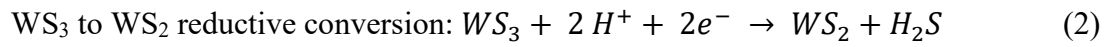
The initial electroadsorption of WS$_3$ moieties (1), a reaction pathway similar to that proposed in $[MoS_4]^{2-}$ anodic electrodeposition,[68][70] is suggested to be followed by either a conversion of WS$_3$ to WS$_2$ (2) or a partial re-dissolution of WS$_3$ (3), the latter allegedly aggravated at faster scan rates. Passivation of the electroactive surface during oxidative adsorption is suggested to occur due to co-deposition of non-conducting S$_8$, whilst partial WS$_3$ to WS$_2$ conversion and S$_8$ cathodic electrodissolution are suggested to provide surface sites susceptible to $[WS_4]^{2-}$ oxidative electroadsorption.
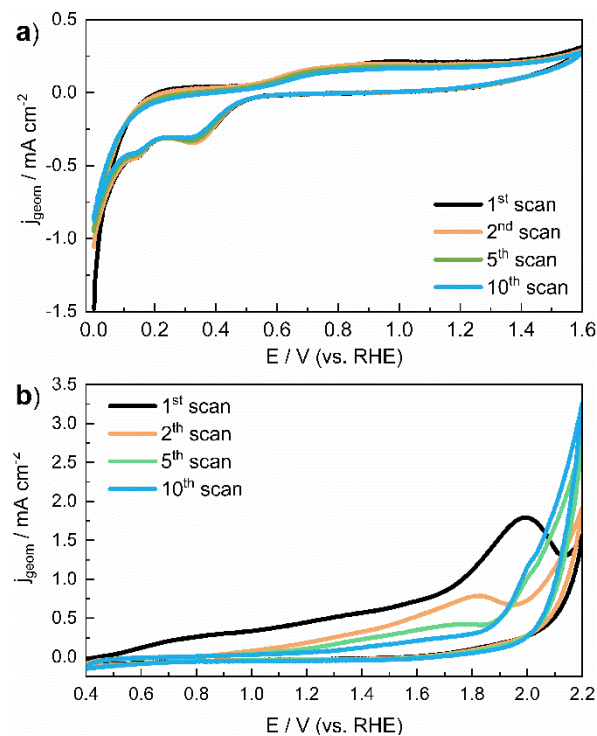
Figure 4. Representative voltammograms obtained on 0.25 cm^2 Si/Cr/Ir electrodes by continuous voltage cycling in a 10 mM $(NH_4)_2[WS_4]$, 0.1 M $NaClO_4$ aqueous electrolyte in the voltage windows a) 0 to 1.6 V and b) 0.4 to 2.2 V vs. RHE (starting potential: 0.4 V). Scan rate: 50 mV s^{-1}.

2.1.2 Electrodeposition strategy and physical characterization of WS$_{3-x}$ decorated Ir electrodes

Having in mind the previous findings, and our aim to selectively passivate the high surface energy, low coordination number Ir sites to retain OER functionality yet minimizing electrodissolution of sputtered polycrystalline Ir, WS$_{3-x}$ decoration was carried out by pulsed electrodeposition (PE) as this approach should trigger both $[WS_4]^{2-}$ oxidative electroadsorption and WS$_3$ to WS$_2$ conversion processes, as shown in deposition mechanism (1) and (2).

11

Preliminary studies were conducted, focusing on applying potential-controlled pulses, anodically within the 1.8 to 2.2 V vs. RHE potential window, and cathodic pulses in the -0.2 to 0.1 V vs. RHE window. These potential windows were selected to evaluate WS_{3-x} nuclei characteristics when pulsing in regions ascribed to the onset, peak potential, and diffusion decay peak regions of both anodic and cathodic processes. In all cases, the high transient currents obtained ($|j_{geom}| > 30$ mA cm^{-2}, see Figure S2a for representative (j_{geom},t) profile) resulted in accelerated electrodissolution of the thermally deposited Ir layer, exposing the underlying Cr and Si layers. As this is undesirable for our application, we opted to perform current-controlled pulses, selecting ±500 µA (ca. ±2 mA cm^{-2}), ±700 µA (ca. ±2.8 mA cm^{-2}) and ±900 µA ca. (±3.6 mA cm^{-2}) as pulse currents. These markedly different values were selected after inspection of the oxidative-reductive CVs shown in Figure 1c (for representative current pulse profiles see Figure S2b), which approximately correspond to experimental currents observed at the onset, peak potential and diffusion-limited voltage regions, respectively. The effect of the pulse timescale and total deposition duration on the WS_{3-x} nuclei size and surface coverage was also assessed. Short (62.5 ms), medium (250 ms) and long (1000 ms) pulses are selected, whilst experiment duration was modified between 1 to 10 minutes.

Morphology characterization of Si/Cr/Ir electrodes before and after reverse pulsed deposition from an aqueous $[WS_4]^{2-}$ bath was performed by SEM. Micrographs of the as-received Si/Cr/Ir surface (Figure 5a-b) show smooth surfaces with cracks within the Ir layer (lengths: 0.5-15 µm, widths: 10-35 nm) range, and Ir grain sizes of 25±7 nm. The observed cracks most probably originate from internal stress/strain of the Ir film during thermal deposition, leading to a corrugated profile: their abundance has been found to vary across the wafers employed. SEM micrographs comparison of Si/Cr/Ir electrodes undergoing pulses of different magnitude for a given pulse duration in an aqueous $[WS_4]^{2-}$ bath are shown in Figure S3. It can be clearly seen

that pulses of higher magnitude applied in shorter experiment durations yield minimal to no observable Ir surface modification relative to its grain size. We hypothesize that higher magnitude pulses lead towards a lower WS_{3-x} nuclei deposition efficiency. Higher currents employed per pulse are expected yield faster depletion rates of the $[WS_4]^{2-}$ species at the electrode-electrolyte interface, and higher fractions of the charge passed allocated to the competing HER/OER processes observed for Ir. Analysis of the micrographs of Si/Cr/Ir electrodes undergoing current pulses of different timescale for a given total experiment duration (Figure S4) show that nuclei size and surface coverage are drastically affected. Longer pulses (1000 ms) yield a higher density of large nuclei, whilst medium and short pulses yield nuclei sizes and coverages beyond the SEM resolution, if even present at all. We believe that for short current pulse timescales the electrodeposition kinetics might not be fast enough to fully take place, i.e. a phenomenon which would primarily contribute to non-faradaic charge-discharge occurring in the µs-ms timescale depending on the experimental time constant.[72] Further insight on the effect of total experiment duration can be gathered by analysis of the micrographs obtained for the ±500 µA pulsed electrodeposited samples (Figure 5c-e and S5). Longer pulse times (≥ 5 min) yield larger WS_{3-x} nuclei and higher surface coverages (average size: 205±70 nm after 10 min, 42±11 nm after 5 min). However, shorter deposition times (≤ 2.5 min) do not yield WS_{3-x} nuclei visible within SEM resolution, due to their foreseen small size. We conclude that WS_{3-x} deposition is maximized in terms of nuclei size and surface coverage when selecting ±500 µA pulse currents, using pulse timescales on the order of 1000 ms and longer total pulse reverse current electrodeposition times, e.g. 10 min.
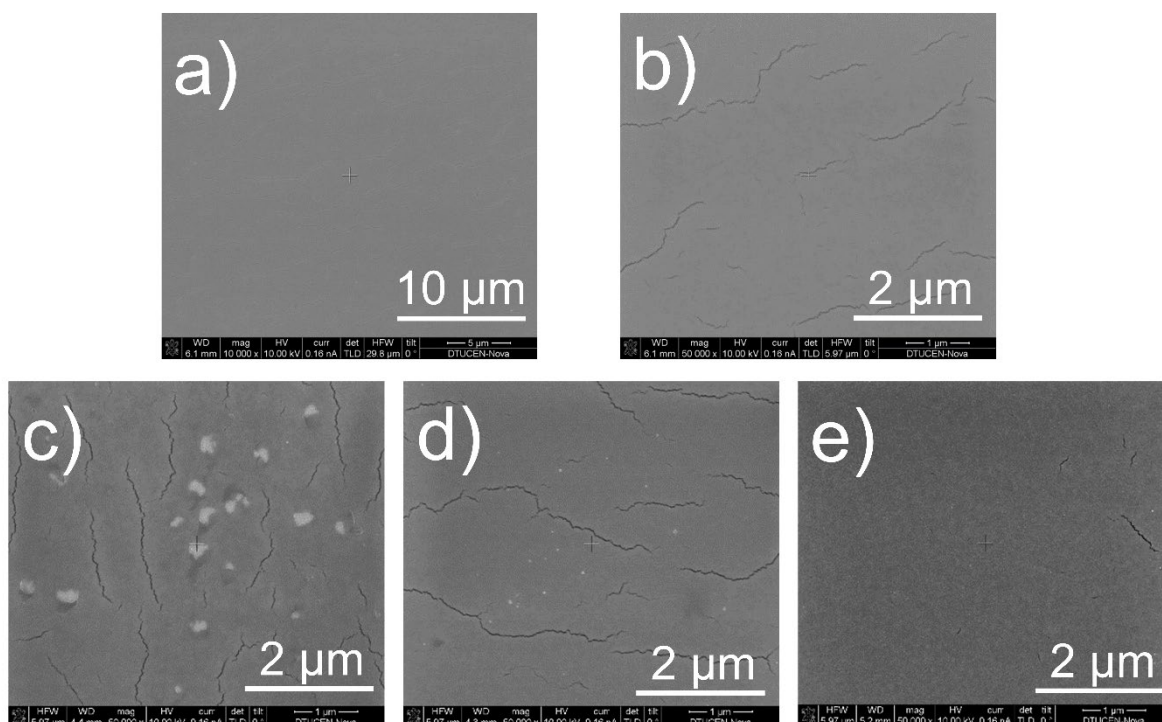
Figure 5. SEM micrographs of as-received Si/Cr/Ir electrodes at a) 10000× and b) 50000× magnification; and Si/Cr/Ir electrodes after undergoing ±500 μA, 1000 ms pulse reverse current electrodeposition experiments for c) 10 min, d) 5 min, e) 1 min. Micrographs image magnification: 50000×.

Thus, two main conclusions can be drawn based on the SEM analysis for Si/Cr/Ir electrodes undergoing reverse pulse current electrodeposition in an aqueous $[WS_4]^{2-}$ bath. First, deposition of WS_{3-x} nuclei seems to occur: amorphous aggregates physically attached to the Ir surface can be identified. Second, the electrodeposition protocol does not seem to significantly modify the inherent Ir surface morphology.

2.2 Electrochemical testing of WS$_{3-x}$ decorated Ir electrodes: oxygen evolution reaction (OER)

2.2.1 Short-term OER testing

The effect of WS$_{3-x}$ pulse reverse current electrodeposition on Ir electrodes towards the OER was investigated (see Experimental for details). In brief, all samples were electrochemically preconditioned until a pseudo-stationary response was obtained, followed by cyclic voltammetry acquisition in the H$_{upd}$ potential region (0.025 to 0.55 V vs. RHE) and OER (1.0 to 1.60 V vs. RHE) voltage windows to evaluate modifications in the electrochemically active surface area (ECSA) corresponding to metallic Ir and OER activity before/after OER stability testing. Short-term stability testing was evaluated by recording chronopotentiograms during 2 hours of the potential required to sustain an anodic current density of 10 mA cm^{-2}, as shown in Figure 6. Compared with as-received Ir, which presents an OER potential of 1.729 ± 0.005 V vs. RHE after 2-hour testing, the WS$_{3-x}$ decorated Ir electrodes generally present slightly higher OER overpotentials. This is expected, as WS$_{3-x}$ is less OER active than pure Ir and its incorporation on the Ir surface will inevitably block some of the highly active Ir OER surface sites, increasing the overall OER overpotential. However, the most relevant metrics to evaluate the passivating effect of WS$_{3-x}$ on Ir electrodes are the variation in OER overpotential (ΔE_{OER}) after short-term testing, and the modifications in the mass activities (OER current normalized by Ir loading) and specific activities (OER current normalized by electrochemically active Ir surface area). For mass and specific activity elucidation, see Section 1.4 ESI.

Trends in the OER activity as a function of the deposition conditions should be first analysed. For medium pulses (250 ms), the slower deposition process compared to other phenomena such as the non-faradaic charge-discharge and other electrochemical restructuring might explain the

initially poor OER performances. If present, WS_{3-x} nuclei should be small and their effect in OER stability under short-term operation will be minor. For Ir samples undergoing long electrodeposition pulses (1000 ms), clearer trends can be found, as the WS_{3-x} deposition occurs more efficiently. When total pulse reverse current electrodeposition times are longer, the samples present gradually improved OER stabilities: this is the case for ±700 µA, and up to 5 mins for ±500 µA. The WS_{3-x} nuclei size seems to be the key factor here: nuclei larger than 50 nm (as is the case for 10 min, ±500 µA pulse reverse deposition) block a higher percentage of the exposed Ir surface, counterproductive for OER.

Among the samples tested, a narrow set (see Table S1 ESI) present greatly improved OER metrics. For instance, ΔE_{OER} was reduced by ca. 20 mV (39 mV vs. 59 mV; sample: ±500 µA, 250 ms, 1 min). As for the mass and specific activities, although WS_{3-x} decorated samples generally presented on-par or worse OER performances prior to stability measurements, these greatly surpassed pristine Ir electrodes after the 2 hour, +10 mA cm^{-2} galvanostatic stability experiments (for representative OER activity voltammograms, see Figure 7a). Best performing samples presented a ca. 1.6 fold (3.1 vs. 1.9 ± 0.3 A mg$_{Ir}^{-1}$ at 1.55 V) and ca. 1.8 fold (1.03 × 10^{-4} vs 5.71 ± 0.1 × 10^{-5} A cm$_{Ir}^{-2}$ at 1.55 V) enhancement in mass and specific activities, respectively.
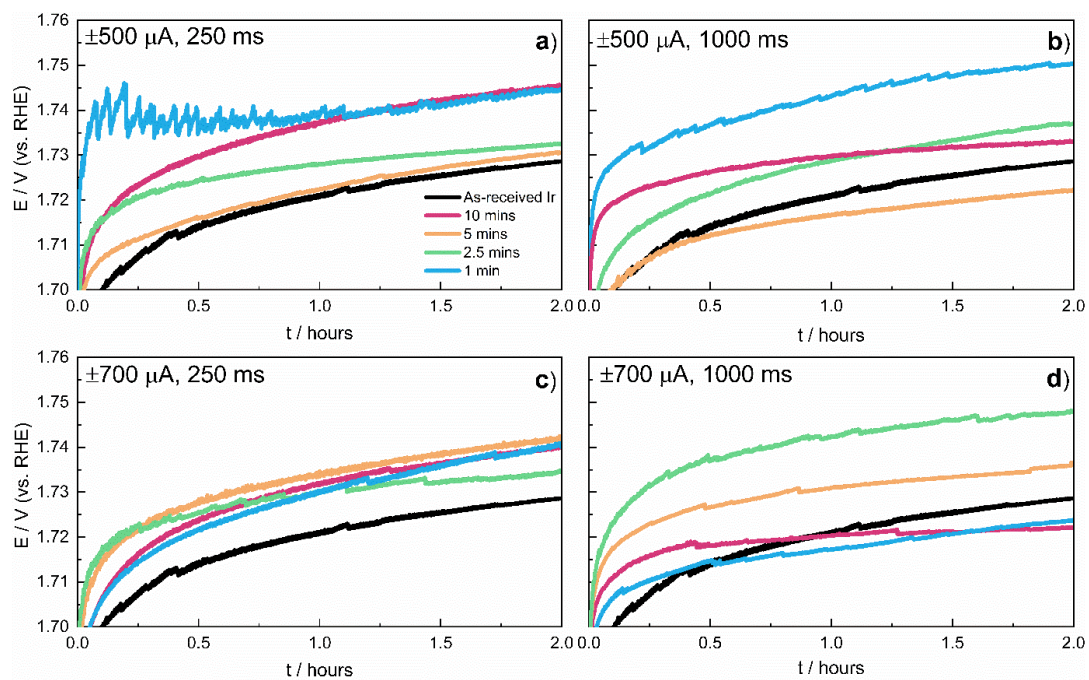
Figure 6. Representative chronopotentiograms recorded for Si/Cr/Ir electrodes before and after undergoing ±500 (a,b) and ±700 µA (c,d) pulse reverse current electrodeposition experiments, to sustain j_{geom}= 10 mA cm^{-2} for 2 h. Labels (total electrodeposition time): as-received (black), 10 min (red), 5 min (orange), 2.5 min (green) and 1 min (blue).

The OER geometric current density values obtained prior to OER stability testing can again be explained by the electrocatalytic inertness of WS_{3-x} nuclei towards the OER. Indeed, the first voltammograms recorded towards OER potentials are markedly different between pristine Ir samples and those decorated with WS_{3-x}, particularly in the pre-OER potential region (1 to 1.4 V vs. RHE) where broad electro-oxidative features were identified (Figure 7b). For pristine Ir, a decreasing anodic current related to the $Ir(OH)_3 \rightleftharpoons IrO(OH)_2$ redox transition up to 1.1 V vs. RHE is still present (tailing of peak III found in Figure 1b),[18] followed by the characteristic oxygen evolution current. Conversely, the WS_{3-x} decorated samples this redox transition is absent, observing instead a broad electro-oxidation peak centred at ca. 1.25 V vs. RHE, followed by OER shifted towards smaller overpotentials.
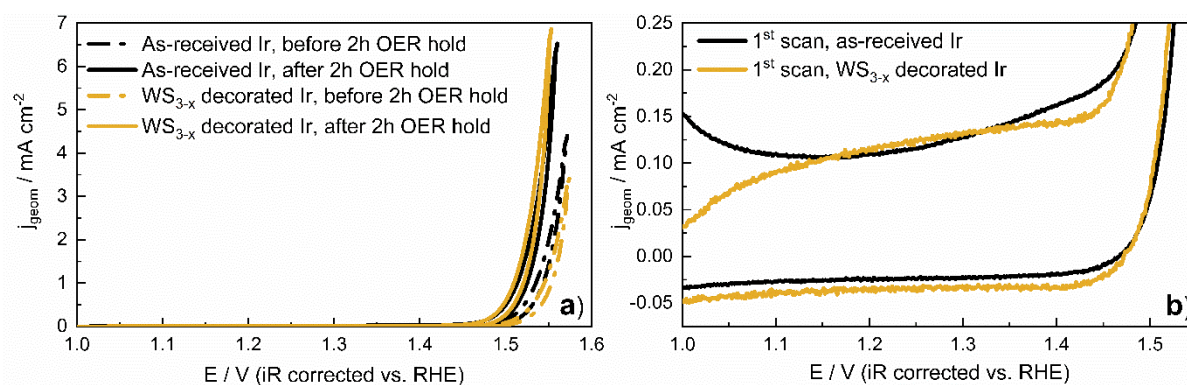
Figure 7. CVs recorded of pristine (black) and WS_{3-x} decorated (± 500 µA, 1000 ms, 5 min,ochre) Si/Cr/Ir electrodes a) before (broken line) and after (solid line) undergoing short-term OER stability experiments: $j_{geom}= 10$ mA cm^{-2} sustained for 2 h; b) first OER voltammograms recorded for pristine and WS_{3-x} decorated (± 700 µA, 250 ms, 10 min). Voltage window: 1.0 to 1.6 V vs. RHE. Electrolyte: 0.1 M $HClO_4$. Scan rate: 10 mV s^{-1}.

We hypothesize that this broad electro-oxidative peak corresponds to the irreversible electro-oxidative conversion of W^{4+} centres in WS_{3-x} nuclei to W^{6+} as found in WO_3.[58] Proof of this conversion can be gathered by analysing the W $4f$ XPS peak originating from the WS_{3-x}

decorated Ir samples after short-term OER testing (Figure 8).The characteristic W $4f_{7/2}{:}4f_{5/2}$ spin-orbit doublet of W^{4+} species, at binding energies of ca. 32.3 and 34.5 eV, is positively shifted after OER testing by ca. 3.7 eV, yielding a doublet centred at 36 and 38.2 eV. These binding energies are characteristic of W^{6+} species, as found in WO_3.[73][74] This conversion is key in Ir stability maximization, as WO_3 is a thermodynamically stable oxide under strongly anodic potentials in acidic media.[60]
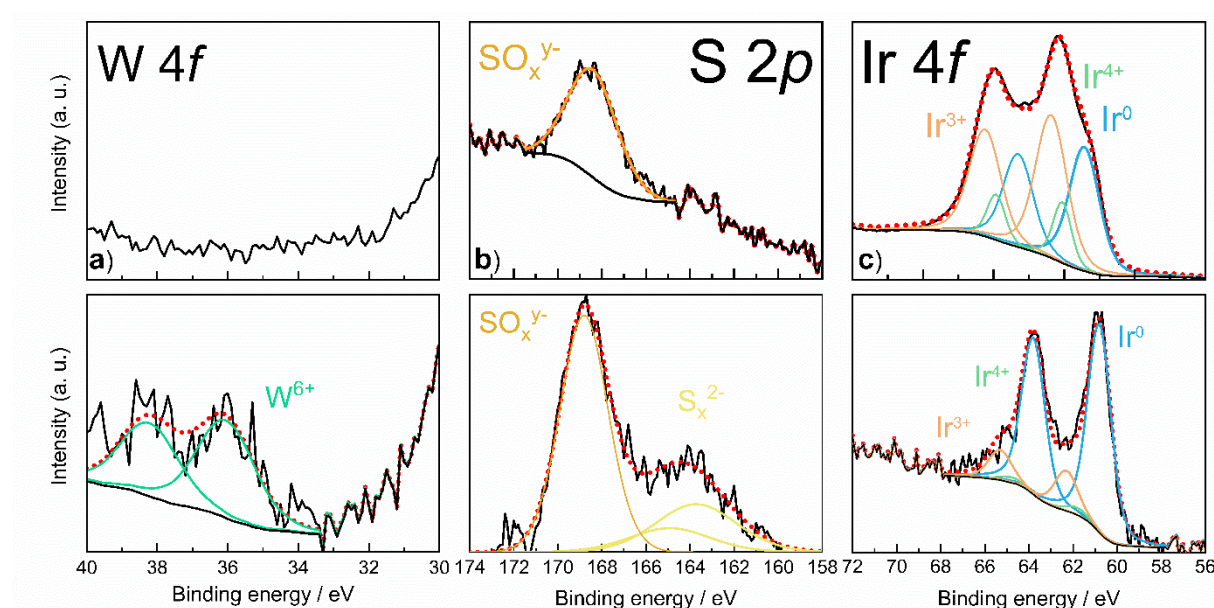
Figure 8. XPS spectra of a) W *4f*, b) S *2p* and c) Ir *4f* for pristine (top) and WS_{3-x} decorated (±500 µA, 1000 ms, 5 min; bottom) Ir samples after undergoing short-term OER stability experiments. Labels: W^{6+} *4f_{7/2:5/2}* (orange), S *2p_{3/2:1/2}* (S^{2-}, yellow), S *2p_{3/2:1/2}* (S_2^{2-}, magenta), S *2p_{3/2:1/2}* (SO_x^{y-}, dark blue), Ir^0 *4f_{7/2:5/2}* (blue), Ir^{4+} *4f_{7/2:5/2}* (green),Ir^{3+} *4f_{7/2:5/2}* (orange), and cumulative spectra (red).

Insights into the origin of the improved OER metrics after 2 h stability testing can be gathered by joint analysis of the electrochemistry, SEM and XPS results. Ir surface roughening, was monitored qualitatively by SEM, and quantitatively by roughness factor measurements (R_f, defined here as ECSA normalized per geometric electrode area),[14] can be correlated with Ir electrodissolution or surface restructuring. Higher R_f, compared with pristine samples, indicate surfaces that present a higher density of Ir sites geometrically accessible to the electrolyte

exposed after Ir dissolution at the surface.[9] SEM micrographs show that pristine Ir samples (Figure S6a) present surfaces with increased grain sizes at longer stability experiments, whereas for WS$_{3-x}$ decorated Ir samples (Figure S6b-d) this surface roughening is less severe. Variation in the density and dimensions of the surface cracks are again related to variability within the Si/Cr/Ir wafers employed. Quantitative comparison of R_f values before OER testing (Table S2) clearly shows higher values for WS$_{3-x}$ decorated Ir samples (R_f range: 33-71) when compared to pristine Ir samples ($R_f = 38 \pm 17$). This would initially suggest that, during the pulse reverse current step of WS$_{3-x}$ electrodeposition, Ir electrodissolution could also occur besides surface restructuring. Indeed, anodic dissolution due to the irreversible conversion of Ir to IrO$_4^{2-}$ via IrO$_x$ formation is known to occur at E > 0.9 V vs. RHE,[16][18] whilst cathodic dissolution occurs at E ≤ 0.1 V vs. RHE due to IrO$_x$ reduction.[75] These potentials are achieved, or surpassed, during electrodeposition. However, the absence of any IrO$_x$ component in the Ir 4f spectrum after cycling in the (NH$_4$)$_2$[WS$_4$] bath (Figure 2c) would suggest otherwise, as the electrochemical growth of hydrous iridium oxide is suppressed (Figure 1a). Thus, although Ir electrodissolution cannot be fully discarded, we believe that increased R_f values after WS$_{3-x}$ decoration are mostly related to electrochemically-induced surface coarsening.

Interestingly, R_f values of WS$_{3-x}$ decorated Ir samples present significantly lower values after OER activity (57-89 vs. 76 ± 7) and OER stability testing (65-94 vs. 86 ± 8) than pristine Ir. This seems to indicate that Ir electrodissolution during OER testing is mitigated once Ir samples have undergone WS$_{3-x}$ decoration. Indeed, after OER stability testing, a 126% relative R_f increase was found for pristine Ir compared with the 15.23 % of the least roughened WS$_{3-x}$ decorated sample (±900 µA, 250 ms, 5 min).

Tafel slope analysis of the voltammograms before and after short-term OER testing (Table S2) provides relevant information regarding the electrode kinetics. In particular, metallic Ir electrodes (covered by a thin anhydrous oxide layer) present Tafel slopes of ca. 66 mV dec^{-1},[18]

whereas electrochemically grown hydrous iridium oxide on metallic Ir present slopes of ca. 40-50 mV dec^{-1}. Lower Tafel slopes are generally found at for metallic Ir surfaces with increasing hydrous oxide layer thicknesses.[76] This Tafel slope dependence on the hydrous oxide layer thickness was ascribed to a modification in the OER rate-determining step,[77] this being a chemical step where the initially unstable electroadsorbed OH species undergo a rearrangement by a surface reaction. [78]

As-received Ir electrodes present with Tafel slopes of 39 ± 2 before, and ~45 ± 2 mV dec^{-1} after OER testing, respectively. These values are close to 40 mV dec^{-1}, indicating that the OER rate-determining step of the tested electrodes is the adsorbed OH species' de-protonation, and that a hydrous iridium oxide overlayer electrochemically grown onto metallic Ir during OER conditioning is the surface species predominantly involved in the OER. With regards to WS$_{3-x}$ decorated samples, Tafel slopes before and after testing range from ~41-48 to ~43-47 mV dec^{-1}, respectively. This suggests that WS$_{3-x}$ decorated samples do not differ greatly from the pristine Ir samples, concluding that the OER mechanism is apparently unaffected by the presence of the WO$_3$ nuclei. However, their somewhat slightly higher values could indicate either the presence of a thinner/less porous hydrous iridium oxide layer or a mitigated electrochemical restructuring, yielding higher stabilities. The latter is experimentally supported by the lower R_f values for decorated samples after testing. Keeping this in mind, the OER mass- and specific activity metrics can now be easily explained. Before OER testing, WS$_{3-x}$ decorated samples present mildly higher mass activity and lower specific activity values with respect to the pristine counterparts, due to their higher surface roughness (higher R_f). On the other hand, improved specific activities obtained after 2 h stability testing show that the enhanced OER current densities and mass activities on WS$_{3-x}$ decorated samples do not stem from surface area effects, as the surface roughening on these samples is attenuated (lower R_f and faintly higher Tafel slopes). Thus, alterations in the Ir surface species must be responsible for the observations.

Comparison of the deconvoluted Ir $4f$ spectra of pristine and WS$_{3-x}$ decorated Ir samples after short-term OER testing shows clear modifications in the surface species present (Figure 8). In contrast with its pristine counterpart, the WS$_{3-x}$ decorated Ir sample retains its predominantly metallic character, with a minor contribution of two additional $4f$ spin-orbit doublets characteristic of Ir^{4+} (ca. 62.5 and 65.5 eV) and Ir^{3+} (ca. 63 and 66 eV) as found in IrO$_2$ or Ir(OH)$_3$, respectively.[79][80] Quantification of the relative atomic photoemission percentages of the deconvoluted components supports this. The relative abundance of the Ir^0: Ir^{3+}: Ir^{4+} species shifts from an atomic % ratio of 40.0:11.0:48.0 in pristine Ir to 81.5:2.8:15.7 at. % after WS$_{3-x}$ decoration. Thus, the acid-insoluble WO$_3$ nuclei mitigate the electro-oxidation of Ir towards higher oxidation states prone to electrodissolution, namely Ir^{3+} [81] as found in the electrochemically generated Ir(OH)$_3$ hydrous oxide. Indeed, the highly-porous hydrous iridium oxide layer present in pristine Ir samples explains then their higher R_f values after OER testing, and also the lower Tafel slopes compared with the WS$_{3-x}$ decorated Ir sample.

2.2.2 Long-term OER testing

Next, we evaluated the OER stability of pristine and WS$_{3-x}$ decorated Ir samples in a protocol analogous to that of Section 2.2.1, but recording chronopotentiograms for 12 hours to monitor changes in the voltage required to sustain an anodic current density of 10 mA cm^{-2} (see Figure 9b). Although previous reports on in-operando scanning flow cell/inductively coupled plasma mass spectrometry (SFC/ICP-MS) indicated that Ir electrodissolution is higher in the transient stage (shorter timescales, i.e. during IrO$_x$ formation) than in the steady-state (longer timescales, $\gg$ 1000 s),[16] the 6-fold longer OER stability testing duration selected is expected to provide more representative information on the passivating effect of WO$_3$ for long-term OER applications.

The OER metrics obtained prior to OER stability testing (for values, see Table S3) mirror those found for the 2 h-tested Ir samples: geometric current densities (0.46-1.88 vs. 2.58 mA cm^{-2} at 1.55 V vs. RHE) and specific activities (1.49-4.20 × 10^{-5} vs. 5.24 × 10^{-5} A cm$_{Ir}^{-2}$ at 1.55 V vs. RHE) are lower for WS$_{3-x}$ decorated than for pristine Ir samples, whilst mass activities are on par or lower (0.165-0.596 vs. 0.56 A mg$_{Ir}^{-1}$ at 1.55 V vs. RHE). After 12 h OER testing, geometric current densities (5.65-7.80 vs. 6.73 mA cm^{-2} at 1.55 V vs. RHE) and mass activities (1.86-2.86 vs. 2.82 A mg$_{Ir}^{-1}$ at 1.55 V vs. RHE) are comparable or lower to those found in pristine Ir electrodes. This would initially suggest, disregarding any contribution from electroactive surface area effects, that the OER activity of the WS$_{3-x}$ decorated (WO$_3$ under OER potentials) Ir electrodes is limited by the passivating effect of the nuclei (for representative OER activity voltammograms, see Figure 9a). However, prominent improvements were found in both R_f and specific activities (Table S4). These metrics enable a more realistic interpretation of the OER stability, as they are normalized by the electroactive area. Improved electrode stabilities will yield lower R_f values, and consequently higher specific activities at a given geometric current density. Namely, relative R_f increases (excluding the ±700 µA, 250 ms, 2.5 min sample) are within 14.8-44.98 % for WS$_{3-x}$ decorated samples compared with the 91.57 % found for pristine Ir. As for specific activities, all WS$_{3-x}$ decorated samples outperform the pristine Ir counterpart, with the best-performing sample (±700 µA, 1000 ms, 10 min) presenting a 1.8-fold increase: 1.30 × 10^{-4} vs. 7.12 × 10^{-5} A cm$_{Ir}^{-2}$ at 1.55 V vs. RHE. Tafel slope analysis of the WS$_{3-x}$ decorated and pristine Ir samples before and after 12 testing follows the same trend found after short-term testing (Table S4). Almost invariable, yet slightly higher values before (39-48 vs. 41 mV dec^{-1}) and after (37-47 vs. 44 mV dec^{-1}) OER operation suggest a slower Ir electrodissolution rate for WS$_{3-x}$ decorated samples. Thus, the presence of WO$_3$ nuclei onto Ir electrodes again results in minimized Ir surface restructuring (mitigated ECSA modifications)

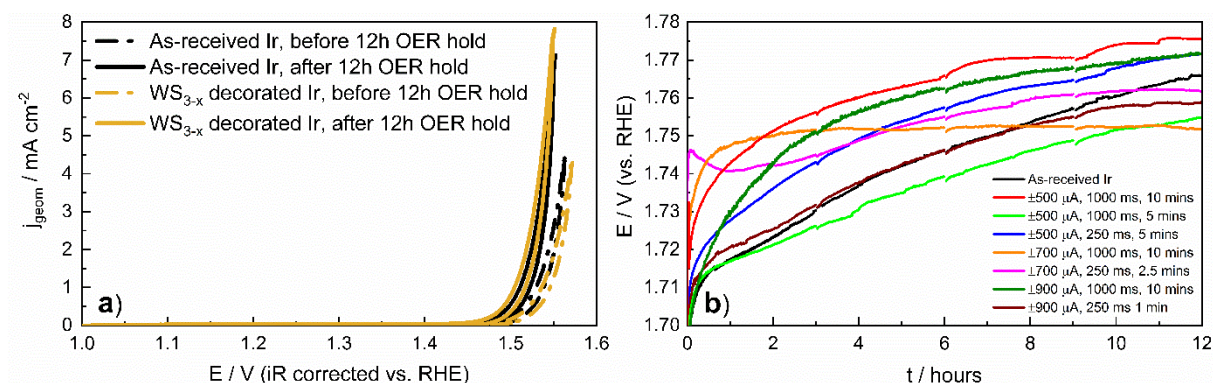and electrodissolution, even under the significantly extended OER operating conditions employed.

Figure 9. CVs recorded at pristine (black) and WS$_{3-x}$ decorated (±500 µA, 1000 ms, 5 min, dark yellow) Si/Cr/Ir electrodes a) before (broken line) and after (solid line) undergoing long-term OER stability experiments: j$_{geom}$= 10 mA cm^{-2} sustained for 12 h. Voltage window: 1.0 to 1.6 V vs. RHE. Scan rate: 10 mV s^{-1}.; b) first OER voltammograms recorded for pristine and WS$_{3-x}$ decorated (±700 µA, 250 ms, 10 min). Electrolyte: 0.1 M HClO$_4$.

The most relevant findings when comparing the results after 12 h and 2h OER stability tests are, strikingly, related to the final OER working potential recorded values (E_{OER,t_f}) and their relative increase versus the starting potential (ΔE_{OER}). Unlike 2 h OER-tested samples, in almost all cases both ΔE_{OER} and E_{OER,t_f} were lower for WS$_{3-x}$ decorated Ir samples than for pristine Ir. (Figure 9b) The improvement, despite of not being numerically large (for the best-performing sample, E_{OER,t_f} = -14 mV, ΔE_{OER} = -43 mV), is foreseen to be amplified, as occurred in our investigations after extending the OER stability testing from 2 to 12 hours, at longer operating conditions due to the extremely flat (E,t) profiles observed. Indeed, the samples presenting improvements in these metrics also present higher Tafel slopes, correlated with slower electrodissolution rates as mentioned previously.[16] Thus, the stabilizing effect of WO$_3$ is not only maintained, but also reinforced, after long-term OER operation conditions, yielding OER metrics which outperform those of pristine Ir surfaces.

Analysis of the Ir surface morphology by SEM micrographs (Figure S6, right column) supports these conclusions. No clear surface modification can be found for WS_{3-x} decorated Ir samples after 12 h OER testing compared with short-term tested samples, whereas the grain size on pristine Ir surfaces coarsens (quantitative evidence is found in R_f elucidation, Table S4).

3. Conclusion

In this study, we have evaluated the viability of an electrochemical decoration process on Ir electrodes based on the decomposition of a $[WS_4]^{2-}$ aqueous precursor to yield amorphous tungsten sulphide (WS_{3-x}) nanoparticles. A preliminary evaluation of the electrochemical features of the $[WS_4]^{2-}$ aqueous bath revealed their analogy with previously reported substrates, indicative of a substrate-independent electrodeposition mechanism. The suppressed inherent Ir electrochemistry as well as the hampered HER and OER catalysis after cycling from oxidative to reductive potentials seems to suggest that both the anodic $[WS_4]^{2-}$ electroadsorption and S co-deposition block the Ir surface sites responsible for proton and hydroxyl adsorption. Cycling within the voltage window comprising the $[WS_4]^{2-}$ anodic and cathodic features yields pseudo-stationary electrochemical responses, contrasting with selective cycling within anodic and cathodic voltage windows, which results in increasingly mitigated or absent $[WS_4]^{2-}$ deposition features, respectively. This conforms to the maximized WS_{3-x} deposition yields previously reported by oxidative-reductive cycling.

The pulse reverse current electrodeposition strategy, selected to satisfy the maximized electrodeposition by co-existing anodic and cathodic processes, has been found to be heavily influenced by both current pulse magnitudes and duration. Low magnitude pulses (e.g. ±500 µA) applied at long timescales (1000 ms) provide the larger WS_{3-x} nuclei and higher coverages,

and vice versa. We hypothesize that at high magnitudes and shorter timescales, $[WS_4]^{2-}$ depletion, competing electrochemical reactions (HER/OER) and sluggish reaction kinetics limit the electrochemically assisted $[WS_4]^{2-}$ decomposition. Longer electrodeposition durations, predictably, yield larger nuclei sizes. Short and long term OER testing experiments show that WS_{3-x} decorated Ir samples present improved OER metrics, namely lower ΔE_{OER}, as well as higher specific activities, than their pristine counterparts, this magnified at longer testing conditions. We hypothesize that the electro-oxidation of WS_{3-x} to the acid-insoluble WO_3 minimizes the electrodissolution of metallic Ir via Ir^{3+} leaching, supported by preliminary XPS measurements and ex-situ imaging. Thus, decoration with corrosion-resistant TMDs is a novel approach towards improving the OER stability of Ir in harsh acidic environments.

4. Experimental

Electrochemical measurements were carried out with a PC-controlled ECi-200 potentiostat/galvanostat using the software EC4U 4.1.90.1 (Nordic Electrochemistry ApS, Denmark), employing a three-electrode thermostatted electrochemical cells (water jacket, 23 ± 2° C). Oxygen-free conditions during electrochemical experimentation were achieved after purging the electrochemical cell or Ar (99.999% purity, ≤ 2 ppm oxygen, Alphagaz 1 Argon), and maintained by applying a positive atmosphere of the inert gas above the electrolyte surface. All electrochemical glassware was cleaned overnight by soaking in an acidified saturated solution of $KMnO_4$ (≥ 99%, crystalline, extra pure, Merck) followed by rinsing in a 1 L aqueous solution containing H_2SO_4 (0.5mL, 95% technical grade, VWR Chemicals) and H_2O_2 (30 mL), and copious rinsing with ultrapure water. The electrochemical glassware was then boiled in ultrapure water no less than three times prior to electrochemical experimentation.

The reference electrode used consisted of an in-house fabricated RHE, obtained by flame sealing the narrow end of a previously snapped Pasteur pipette containing a protruding 1 mm

Pt wire (Alfa Aesar), which is rinsed and filled up with the same electrolyte as used for electrochemical experiments (for this work either 0.1 M NaClO$_4$ or 0.1 M HClO$_4$) and then inserted onto a glass vessel. A fritted double junction for WS$_x$ electrodeposition or a Luggin capillary for OER experiments, both filled with analogous electrolyte to prevent electrolyte cross-contamination and RHE voltage drift. A two-electrode electrochemical cell configuration to undergo in-situ hydrogen production at the Pasteur reservoir by electrolysis (WE potential: -2 V vs. RHE, 5-10 mins) was achieved by use of a Pt wire counter electrode (CE). Experimental deviations in the RHE value were accounted for by acquisition of 10 cyclic voltammograms from -0.25 to 0.15 Vvs. RHE (starting potential: 0.05 V vs. RHE) after 10 minutes purging with H$_2$ to reach solution saturation. Real RHE values were elucidated by averaging the experimental voltage values obtained at 0 A for the 10th forward/backward scan. The counter electrodes used in this work are 3 mm glassy carbon rods to prevent foreseeable dissolution and re-deposition found when employing Pt-based counter electrodes.

Tungsten sulphide (WS$_{3-x}$) was deposited onto Si (0.5 mm)/Si thermal oxidation layer (1 μm)/ Cr (10 nm)/Ir (100 nm) substrates prepared by sputtering deposition and mechanical dicing (5 ×15 mm, IMB-CNM, Universitat Autònoma de Barcelona, Spain) by electrochemical deposition from a freshly-prepared, deaerated electrolyte solution containing 10mM (NH$_4$)$_2$[WS$_4$] (99.9% trace metals basis, Sigma-Aldrich) and 0.1 M NaClO$_4$ (≥99.0% AnalaR Normapur, VWR Chemicals). Prior to use, Si/Cr/Ir chips were ultrasonicated sequentially in acetone (×3, 3 min), isopropanol (2 min) and finally rinsed in ultrapure water to eliminate the polymeric resin coated onto the substrates, used for preventing particle contamination from mechanical dicing and surface scratching during wafer transportation. A deposition area on Si/Cr/Ir chips (5×5 mm) was selectively exposed to the electrolyte by insulating the remaining working electrode surface with hydrophobic Teflon tape. Electrodeposition was carried out under quiescent conditions to prevent alterations in the deposition rate from the effects of forced

convection. Preliminary WS$_{3-x}$ deposition studies were performed by depositing thin films by continuous cyclic voltammetry experiments within the -0.4 to 2.5 V vs. RHE voltage window. Galvanostatic pulsed electrodeposition was performed by symmetrically alternating the working electrode current intensity in the 500-900 μA current range. Several current pulse time durations (0.0625, 0.125, 0.25, 0.5 and 1 s) and total electrodeposition times (1, 2.5, 5 and 10 min) were employed to evaluate modifications in WS$_{3-x}$ nuclei size and coverages.

All Ir samples were preconditioned prior to oxygen evolution reaction (OER) electrochemical testing by recording 20 cyclic voltammograms from 0 to 0.7 V vs. RHE at a voltage scan rate of 50 mV s^{-1}. This electrochemical preconditioning was followed by the acquisition of 20 cyclic voltammograms from 0.025 to 0.55 V vs. RHE at a voltage scan rate of 50 mV s^{-1}. This aims to evaluate the electrochemical active surface area (ECSA) of the Ir electrodes, and is repeated before/after any OER testing measurement. ECSA is estimated for the 20th cycle by integrating the hydrogen desorption region from 0.06 V to the potential where the hydrogen desorption concludes. Next, OER activity is evaluated by the acquisition of 10 cyclic voltammograms from 1 to 1.6 V vs. RHE at a voltage scan rate of 10 mV s^{-1}. After the corresponding repetition of the ECSA measurements, Ir electrodes OER stability is monitored by a short term (2 hours) or long term (12 hours) chronopotentiometry experiment set to monitor the overpotential required to sustain a constant OER geometric current density of 10 mA cm^{-2}. For long term stability experiments, a 1000 rpm stirring rate was employed. After all OER stability measurements, ECSA and OER activity measurements (the latter only for 3 cycles) were recorded to evaluate modifications in the Ir electrodes surface and electrocatalysis. *iR* compensation corrections on all voltammograms were accounted for by software-assisted subtraction (EC4 View, version 1.2.68.1) of the high-frequency EIS component of the Nyquist plot (-Z''= 0).

All oxygen evolution experiments were performed in a 0.1 M HClO$_4$ electrolyte (70%, Suprapur®, Merck), and freshly prepared with ultrapure water (resistivity not less than 18.2 MΩ·cm, Millipore Milli-Q Direct 8).

Physical characterization:

FEG-SEM micrographs were acquired to determine the surface modification and roughening upon electrochemical degradation on WS$_{3-x}$-modified Ir electrodes. A FEI Nova NanoSEM 600 microscope (Thermo Fisher Scientific, USA) was operated under electron accelerating voltages of 10 kV, spot sizes of 3.5 μm and beam currents of 0.16 mA at the Center for Electron Nanoscopy (DTU, Valby, Denmark).

XPS measurements were performed with a Thermo Scientific Theta Probe employing a microfocused monochromatic aluminium X-ray source (Al Kα, 1486.6 eV, 12 kV), a charge neutralizer filament to prevent surface charging, and working pressures below 5×10^{-9} mbar. Three independent and non-overlapping XPS analysis positions were acquired, using spot 400 × 800 μm on each sample. For low resolution survey spectra, 100 eV pass energies and 1 eV step sizes were employed (dwell time: 10 ms), whereas for element spectra pass energies and step sizes of 100 eV and 0.1 eV were selected (dwell time: 100 ms). All element spectra were energy-corrected to the adventitious C 1s peak set to 284.6 eV, and processed using the CASA XPS software (version 2.3.18PR1.0).

For high resolution spectra peak deconvolution, Gaussian-Lorentzian (30) and Doniach-Šunjić modified Gaussian-Lorentzian lineshapes were employed for S *2p* and W *4f*/Ir *4f*, respectively. S 2p spectra were fitted by applying a 2:1 area ratio constraint and 1.2 eV separation on the $2p_{3/2:1/2}$ spin-orbit doublets,[82]–[84] whereas W *4f* and Ir *4f* spectra were deconvoluted by applying a 2.17 eV and 3.0 eV $4f_{7/2:5/2}$ spin-orbit doublet separation, respectively, and a 4:3 area ratio constraint.[79]

Supporting Information

Supporting Information is available from the Wiley Online Library or from the author.

References

[1]   S. Ardo, D. Fernandez Rivas, M.A. Modestino, V. Schulze Greiving, F.F. Abdi, E. Alarcon Llado, V. Artero, K. Ayers, C. Battaglia, J.-P. Becker, D. Bederak, A. Berger, F. Buda, E. Chinello, B. Dam, V. Di Palma, T. Edvinsson, K. Fujii, H. Gardeniers, H. Geerlings, S.M. H. Hashemi, S. Haussener, F. Houle, J. Huskens, B.D. James, K. Konrad, A. Kudo, P.P. Kunturu, D. Lohse, B. Mei, E.L. Miller, G.F. Moore, J. Muller, K.L. Orchard, T.E. Rosser, F.H. Saadi, J.-W. Schüttauf, B. Seger, S.W. Sheehan, W.A. Smith, J. Spurgeon, M.H. Tang, R. van de Krol, P.C.K. Vesborg, P. Westerik, *Energy Environ. Sci.* **2018**, *11*, 2768.

[2]   B. Parkinson, *ACS Energy Lett.* **2016**, *1*, 1057.

[3]   I. Staffell, D. Scamman, A. Velazquez Abad, P. Balcombe, P.E. Dodds, P. Ekins, N. Shah, K.R. Ward, *Energy Environ. Sci.* **2019**, *12*, 463.

[4]   S. Sharma, S.K. Ghoshal, *Renew. Sustain. Energy Rev.* **2015**, *43*, 1151.

[5]   S. Chu, A. Majumdar, *Nature* **2012**, *488*, 294.

[6]   K. Ayers, N. Danilovic, R. Ouimet, M. Carmo, B. Pivovar, M. Bornstein, *Annu. Rev. Chem. Biomol. Eng.* **2019**, *10*, 219.

[7]   K. Zeng, D. Zhang, *Prog. Energy Combust. Sci.* **2010**, *36*, 307.

[8]   H.A. Miller, K. Bouzek, J. Hnat, S. Loos, C.I. Bernäcker, T. Weißgärber, L. Röntzsch, J. Meier-Haack, *Sustain. Energy Fuels* **2020**, *4*, 2114.

[9]   C. Spöri, J.T.H. Kwan, A. Bonakdarpour, D.P. Wilkinson, P. Strasser, *Angew. Chemie - Int. Ed.* **2017**, *56*, 5994.

[10]   M. Carmo, D.L. Fritz, J. Mergel, D. Stolten, *Int. J. Hydrogen Energy* **2013**, *38*, 4901.

[11]   I. Katsounaros, S. Cherevko, A.R. Zeradjanin, K.J.J. Mayrhofer, *Angew. Chemie - Int. Ed.* **2014**, *53*, 102.

[12]   T. Reier, H.N. Nong, D. Teschner, R. Schlögl, P. Strasser, *Adv. Energy Mater.* **2017**, *7*.

[13]   E. Fabbri, T.J. Schmidt, *ACS Catal.* **2018**, *8*, 9765.

[14]   C.C.L. McCrory, S. Jung, I.M. Ferrer, S. Chatman, J.C. Peters, T.F. Jaramillo, *J. Am. Chem. Soc.* **2015**, *137*, 4347.

[15]   P.C.K. Vesborg, T.F. Jaramillo, *RSC Adv.* **2012**, *2*, 7933.

[16]   S. Cherevko, A.R. Zeradjanin, A.A. Topalov, N. Kulyk, I. Katsounaros, K.J.J. Mayrhofer, *ChemCatChem* **2014**, *6*, 2219.

[17]   S. Cherevko, S. Geiger, O. Kasian, N. Kulyk, J.-P. Grote, A. Savan, B.R. Shrestha, S.

Merzlikin, B. Breitbach, A. Ludwig, K.J.J. Mayrhofer, *Catal. Today* **2016**, *262*, 170.

[18] S. Cherevko, S. Geiger, O. Kasian, A. Mingers, K.J.J. Mayrhofer, *J. Electroanal. Chem.* **2016**, *773*, 69.

[19] H. Yu, L. Bonville, J. Jankovic, R. Maric, *Appl. Catal. B Environ.* **2020**, *260*, 118194.

[20] A. Weiß, A. Siebel, M. Bernt, T.-H. Shen, V. Tileli, H.A. Gasteiger, *J. Electrochem. Soc.* **2019**, *166*, F487.

[21] S. Geiger, O. Kasian, M. Ledendecker, E. Pizzutilo, A.M. Mingers, W.T. Fu, O. Diaz-Morales, Z. Li, T. Oellers, L. Fruchter, A. Ludwig, K.J.J. Mayrhofer, M.T.M. Koper, S. Cherevko, *Nat. Catal.* **2018**, *1*, 508.

[22] S. Geiger, O. Kasian, B.R. Shrestha, A.M. Mingers, K.J.J. Mayrhofer, S. Cherevko, *J. Electrochem. Soc.* **2016**, *163*, F3132.

[23] N. Danilovic, R. Subbaraman, K.C. Chang, S.H. Chang, Y.J. Kang, J. Snyder, A.P. Paulikas, D. Strmcnik, Y.T. Kim, D. Myers, V.R. Stamenkovic, N.M. Markovic, *J. Phys. Chem. Lett.* **2014**, *5*, 2474.

[24] T. Reier, M. Oezaslan, P. Strasser, *ACS Catal.* **2012**, *2*, 1765.

[25] T. Weber, T. Ortmann, D. Escalera-López, M.J.S. Abb, B. Mogwitz, S. Cherevko, M. Rohnke, H. Over, *ChemCatChem* **2020**, *12*, 855.

[26] H. Jin, Y. Hong, J. Yoon, A. Oh, N.K. Chaudhari, H. Baik, S.H. Joo, K. Lee, *Nano Energy* **2017**, *42*, 17.

[27] S. Choi, J. Park, M.K. Kabiraz, Y. Hong, T. Kwon, T. Kim, A. Oh, H. Baik, M. Lee, S.M. Paek, S. Il Choi, K. Lee, *Adv. Funct. Mater.* **2020**, *30*, 1.

[28]   S.M. Alia, S. Shulda, C. Ngo, S. Pylypenko, B.S. Pivovar, *ACS Catal.* **2018**, *8*, 2111.

[29]   F. Lv, J. Feng, K. Wang, Z. Dou, W. Zhang, J. Zhou, C. Yang, M. Luo, Y. Yang, Y. Li, P. Gao, S. Guo, *ACS Cent. Sci.* **2018**, *4*, 1244.

[30]   A.W. Jensen, G.W. Sievers, K.D. Jensen, J. Quinson, J.A. Arminio-Ravelo, V. Brüser, M. Arenz, M. Escudero-Escribano, *J. Mater. Chem. A* **2020**, *8*, 1066.

[31]   T. Reier, Z. Pawolek, S. Cherevko, M. Bruns, T. Jones, D. Teschner, S. Selve, A. Bergmann, H.N. Nong, R. Schlögl, K.J.J. Mayrhofer, P. Strasser, *J. Am. Chem. Soc.* **2015**, *137*, 13031.

[32]   H.N. Nong, T. Reier, H.S. Oh, M. Gliech, P. Paciok, T.H.T. Vu, D. Teschner, M. Heggen, V. Petkov, R. Schlögl, T. Jones, P. Strasser, *Nat. Catal.* **2018**, *1*, 841.

[33]   C. Spöri, P. Briois, H.N. Nong, T. Reier, A. Billard, S. Kühl, D. Teschner, P. Strasser, *ACS Catal.* **2019**, *9*, 6653.

[34]   A.L. Strickler, R.A. Flores, L.A. King, J.K. Nørskov, M. Bajdich, T.F. Jaramillo, *ACS Appl. Mater. Interfaces* **2019**, *11*, 34059.

[35]   H.S. Oh, H.N. Nong, T. Reier, A. Bergmann, M. Gliech, J. Ferreira De Araújo, E. Willinger, R. Schlögl, D. Teschner, P. Strasser, *J. Am. Chem. Soc.* **2016**, *138*, 12552.

[36]   H.S. Oh, H.N. Nong, T. Reier, M. Gliech, P. Strasser, *Chem. Sci.* **2015**, *6*, 3321.

[37]   A. Hartig-Weiss, M. Miller, H. Beyer, A. Schmitt, A. Siebel, A.T.S. Freiberg, H.A. Gasteiger, H.A. El-Sayed, *ACS Appl. Nano Mater.* **2020**, *3*, 2185.

[38]   D. Böhm, M. Beetz, M. Schuster, K. Peters, A.G. Hufnagel, M. Döblinger, B. Böller, T. Bein, D. Fattakhova-Rohlfing, *Adv. Funct. Mater.* **2020**, *30*, 1906670.

[39]   T. Reier, D. Teschner, T. Lunkenbein, A. Bergmann, S. Selve, R. Kraehnert, R. Schlögl, P. Strasser, *J. Electrochem. Soc.* **2014**, *161*, F876.

[40]   C. Van Pham, M. Bühler, J. Knöppel, M. Bierling, D. Seeberger, D. Escalera-López, K.J.J. Mayrhofer, S. Cherevko, S. Thiele, *Appl. Catal. B Environ.* **2020**, *269*, 118762.

[41]   S. Geiger, O. Kasian, A.M. Mingers, K.J.J. Mayrhofer, S. Cherevko, *Sci. Rep.* **2017**, *7*, 3.

[42]   S. Back, K. Tran, Z.W. Ulissi, *ACS Appl. Mater. Interfaces* **2020**, *12*, 38256.

[43]   Z. Wang, Y.-R. Zheng, I. Chorkendorff, J.K. Nørskov, *ACS Energy Lett.* **2020**, *5*, 2905.

[44]   J. Kim, P.C. Shih, K.C. Tsao, Y.T. Pan, X. Yin, C.J. Sun, H. Yang, *J. Am. Chem. Soc.* **2017**, *139*, 12076.

[45]   M. Blasco-Ahicart, J. Soriano-Lopez, J.J. Carbo, J.M. Poblet, J.R. Galan-Mascaros, *Nat. Chem.* **2018**, *10*, 24.

[46]   M. Escudero-Escribano, A.F. Pedersen, E.A. Paoli, R. Frydendal, D. Friebel, P. Malacrida, J. Rossmeisl, I.E.L. Stephens, I. Chorkendorff, *J. Phys. Chem. B* **2018**, *122*, 947.

[47]   S. Kumari, B.P. Ajayi, B. Kumar, J.B. Jasinski, M.K. Sunkara, J.M. Spurgeon, *Energy Environ. Sci.* **2017**, *10*, 2432.

[48]   A.F. Pedersen, M. Escudero-Escribano, B. Sebok, A. Bodin, E. Paoli, R. Frydendal, D. Friebel, I.E.L. Stephens, J. Rossmeisl, I. Chorkendorff, A. Nilsson, *J. Phys. Chem. B* **2018**, *122*, 878.

[49]   B. Vanrenterghem, M. Bele, F.R. Zepeda, M. Šala, N. Hodnik, T. Breugelmans, *Appl.*

Catal. B Environ. **2018**, *226*, 396.

[50] J. Kim, J.E. Dick, A.J. Bard, *Acc. Chem. Res.* **2016**, *49*, 2587.

[51] M. Zhou, J.E. Dick, A.J. Bard, *J. Am. Chem. Soc.* **2017**, *139*, 17677.

[52] P. Sebastián-Pascual, I. Jordão Pereira, M. Escudero-Escribano, *Chem. Commun.* **2020**, *56*, 13261.

[53] M.S. Chandrasekar, M. Pushpavanam, *Electrochim. Acta* **2008**, *53*, 3313.

[54] S.M. Tan, M. Pumera, *Chem. - A Eur. J.* **2017**, *23*, 8510.

[55] S.M. Tan, M. Pumera, *ACS Appl. Mater. Interfaces* **2016**, *8*, 3948.

[56] S.M. Tan, M. Pumera, *ACS Appl. Mater. Interfaces* **2017**, *9*, 41955.

[57] D. Escalera-López, R. Griffin, M. Isaacs, K. Wilson, R.E. Palmer, N. V. Rees, *Electrochem. Commun.* **2017**, *81*, 106.

[58] A.Y.S. Eng, A. Ambrosi, Z. Sofer, P. Simek, M. Pumera, *ACS Nano* **2014**, *8*, 12185.

[59] M. Zafir Mohamad Nasir, Z. Sofer, M. Pumera, *ChemElectroChem* **2015**, *2*, 1713.

[60] M. Pourbaix, *Altas of Electrochemical Equilibrium in Aqueous Solutions*, Pergamon Press, New York **1966**.

[61] K. Kondo, Y. Ikeda, M. Yokoi, *J. Electrochem. Soc.* **2015**, *162*, D218.

[62] J. Gao, X. Huang, W. Cai, Q. Wang, C. Jia, B. Liu, *ACS Appl. Mater. Interfaces* **2020**, *12*, 25991.

[63] J. Juodkazyte, B. Šebeka, I. Valsiunas, K. Juodkazis, *Electroanalysis* **2005**, *17*, 947.

[64]   R. Kötz, C. Barbero, O. Haas, *J. Electroanal. Chem.* **1990**, *296*, 37.

[65]   M.A. Petit, V. Plichon, *J. Electroanal. Chem.* **1998**, *444*, 247.

[66]   T.E. Fonseca, M.I. Lopes, M.T.C. Portela, *J. Electroanal. Chem.* **1996**, *415*, 89.

[67]   D. Escalera-López, Z. Lou, N. V. Rees, *Adv. Energy Mater.* **2019**, *9*.

[68]   D. Merki, S. Fierro, H. Vrubel, X. Hu, *Chem. Sci.* **2011**, *2*, 1262.

[69]   D. Merki, H. Vrubel, L. Rovelli, S. Fierro, X. Hu, *Chem. Sci.* **2012**, *3*, 2515.

[70]   H. Vrubel, X. Hu, *ACS Catal.* **2013**, *3*, 2002.

[71]   B. Łosiewicz, R. Jurczakowski, A. Lasia, *Electrochim. Acta* **2017**, *225*, 160.

[72]   A.J. Bard, L.R. Faulkner, *Electrochemical Methods: Fundamentals and Applications*, John Wiley And Sons Ltd., New York **2001**.

[73]   A. Katrib, F. Hemming, P. Wehrer, L. Hilaire, G. Maire, *J. Electron Spectros. Relat. Phenomena* **1995**, *76*, 195.

[74]   A.P. Shpak, A.M. Korduban, L.M. Kulikov, T. V. Kryshchuk, N.B. Konig, V.O. Kandyba, *J. Electron Spectros. Relat. Phenomena* **2010**, *181*, 234.

[75]   P. Jovanovič, N. Hodnik, F. Ruiz-Zepeda, I. Arčon, B. Jozinović, M. Zorko, M. Bele, M. Šala, V.S. Šelih, S. Hočevar, M. Gaberšček, *J. Am. Chem. Soc.* **2017**, *139*, 12837.

[76]   S. Cherevko, S. Geiger, O. Kasian, A. Mingers, K.J.J. Mayrhofer, *J. Electroanal. Chem.* **2016**, *774*, 102.

[77]   S. Gottesfeld, S. Srinivasan, *J. Electroanal. Chem.* **1978**, *86*, 89.

[78]   L.A. De Faria, J.F.C. Boodts, S. Trasatti, *J. Appl. Electrochem.* **1996**, *26*, 1195.

[79]   V. Pfeifer, T.E. Jones, J.J. Velasco Vélez, C. Massué, R. Arrigo, D. Teschner, F. Girgsdies, M. Scherzer, M.T. Greiner, J. Allan, M. Hashagen, G. Weinberg, S. Piccinin, M. Hävecker, A. Knop-Gericke, R. Schlögl, *Surf. Interface Anal.* **2016**, *48*, 261.

[80]   S.J. Freakley, J. Ruiz-Esquius, D.J. Morgan, *Surf. Interface Anal.* **2017**, *49*, 794.

[81]   O. Kasian, J.P. Grote, S. Geiger, S. Cherevko, K.J.J. Mayrhofer, *Angew. Chemie - Int. Ed.* **2018**, *57*, 2488.

[82]   H.W. Wang, P. Skeldon, G.E. Thompson, *Surf. Coatings Technol.* **1997**, *91*, 200.

[83]   W. Grunert, A.Y. Stakheev, R. Feldhaus, K. Anders, E.S. Shpiro, K.M. Minachev, *J. Phys. Chem.* **1991**, *95*, 1323.

[84]   G.C. Stevens, T. Edmonds, *J. Catal.* **1975**, *37*, 544.